A 3D Mathematical Breast Texture Model with Parameters Automatically Inferred from Clinical Breast CT Images

Zhijin Li, Ann-Katherine Carton, Serge Muller, Thomas Almecija, Pablo Milioni de Carvalho, Agnès Desolneux

A 3D Mathematical Breast Texture Model with Parameters Automatically Inferred from Clinical Breast CT Images

Zhijin Li, Ann-Katherine Carton, Serge Muller, Thomas Almecija, Pablo Milioni de Carvalho, and Agnès Desolneux

***Abstract*— A numerical realistic 3D anthropomorphic breast model is useful for evaluating breast imaging applications. A method is proposed to model small and medium-scale fibroglandular and intra-glandular adipose tissues observed in the center part of clinical breast CT images. The method builds upon a previously proposed model formulated as stochastic geometric processes with mathematically tractable parameters. In this work, the medium-scale parameters were automatically and objectively inferred from breast CT images. We hypothesized that a set of random ellipsoids exhibiting cluster interaction is representative to model the medium-scale intra-glandular adipose compartments. The ellipsoids were reconstructed using a multiple birth, death and shift algorithm. Then, a Matérn cluster process was used to fit the reconstructed ellipsoid centers. Finally, distributions of the ellipsoid shapes and orientations were estimated using maximum likelihood estimators. Feasibility was demonstrated on 16 volumes of interests (VOI).**

To assess the realism of the 3D breast texture model, β and LFE metrics computed in simulated projection images of simulated texture realizations and clinical images were compared. Visual realism was illustrated.

For 12 out of 16 VOIs, our hypothesis on clustering interaction process is confirmed. The average β values from simulated texture images (3.7 to 4.2) of the 12 different VOIs are higher than the average β value from 2D clinical images (2.87). LFE of simulated texture images and clinical mammograms are similar. Compared to our previous model, whereby simulation parameters were based upon empirical observations, our inference method substantially augments the ability to generate textures with higher visual realism and larger morphological variety.

***Index Terms*— X-ray breast imaging, virtual clinical trials, 3D breast texture model, stochastic geometry, statistical parameter inference.**

I. Introduction and motivation

This research was partially funded by the French national association for research and technology (ANRT) under the CIFRE grant n°2013/1052.

Zhijin Li is with GE Healthcare France, Buc, 78530, France (e-mail: jonathan.lizhijin@icloud.com).

Ann-Katherine Carton is with GE Healthcare France, Buc, 78530, France (e-mail: ann-katherine.carton@ge.com).

Serge Muller is with GE Healthcare France, Buc, 78530, France (e-mail: serge.muller@free.fr).

Thomas Almecija is with GE Renewable Energy France, Boulogne-Billancourt, 92100, France (e-mail: thomas.almecija@ge.com).

Pablo Milioni de Carvalho is with GE Healthcare France, Buc, 78530, France (e-mail: pablo.milioni@ge.com).

Agnès Desolneux is with Centre Borelli, Ecole Normale Supérieure Paris-Saclay, 91190 Gif-sur-Yvette, France. (e-mail: agnes.desolneux@ens-paris-saclay.fr).

A 3D anthropomorphic software model of the breast may serve as a useful tool in the development and performance evaluation of breast x-ray imaging applications [1]–[6]. To be effective, a 3D anthropomorphic software model of the breast must be realistic for the envisioned task.

An overview of the advances of anthropomorphic breast phantoms primarily used in breast x-ray imaging applications was recently published by Glick and Ikejimba [7]. Three types of 3D phantoms have been proposed. First, clinical image-based phantoms are in essence reconstructed clinical images from breast CT acquisitions whereby different tissue types are assigned using a segmentation algorithm [8]–[10]. Secondly, mathematical phantoms use mathematical models to define the various anatomical components of the breast [11]–[25]. Thirdly, hybrid phantoms combine the two previous approaches; clinical image-based phantoms are enriched with mathematically defined anatomical components [26]. As an alternative to 3D breast phantoms, Bochud *et al.* [27] and Castella *et al.* [28] developed the *clustered lumpy backgrounds* (CLB), a mathematical model using elements of stochastic geometry to synthesize stationary, random 2D mammography texture images. Because of its 2D nature, the CLB is only appropriate to evaluate 2D mammography applications [29] and not for 3D imaging applications such as digital breast tomosynthesis (DBT) and breast CT. A 3D adaptation of the CLB has been explored [30].

Each of the above phantoms offer advantages and have limitations in terms of mathematical traceability, the capability to generate independent random realizations, morphological variability with respect to the population of women being imaged and the realism of images simulated from these breast phantoms compared to clinical images. In particular, simulated x-ray images of 3D clinical image-based phantoms have high visual realism, but they lack finer details due to the image acquisition and segmentation process. On the other hand, the anatomical structures in mathematical phantoms often have a geometric appearance. To design VCT that will answer clinical questions, it is essential to understand what level of realism is needed depending on the VCT objective. Also, knowledge of the realism constraints of the breast phantoms is key. Today, there is no clear answer on how to validate phantom realism.

Phantom image realism has been extensively assessed by statistical image properties [17], [31]–[33] and to a lesser extent by psychophysical experiments [25], [34], [35]. The more extensive reporting using statistical image properties can be attributed to the practicality of the objective measures, while psychophysical experiments involving humans are time consuming.

Statistical breast image properties have traditionally been characterized by the power spectral index β, a second order metric that depends on the slope of the image power spectrum [20], [31], [32]. Hereby it is assumed that the image texture is locally stationary and has a power spectrum completely characterized by a power-law function, which has been observed in clinical screen-film mammography [31], full field digital mammography (FFDM) [36], DBT [37] and breast CT images [38]. Despite that β contains useful information regarding the breast texture, it does not fully capture the texture characteristics. Phantom images and clinical images with the same β value may have a very different visual appearance [17] [33]. According to Abbey *et al.* [33], the power spectral index should be considered a necessary condition for phantom realism, but not a sufficient condition. To describe image texture more fully, Abbey *et al.* [17] proposed the Laplacian Fractional Entropy (LFE), a higher-order non-Gaussian statistical metric. LFE is based upon the response histograms obtained by convolving the image by Gabor filters representative of receptive fields in the virtual cortex. LFE is the entropy of a response histogram relative to the expected response histogram from a Gaussian process. LFE is a measure of to which extent a response histogram deviates from a Gaussian form. Preliminary results have demonstrated the usefulness of LFE to differentiate clinical and phantom x-ray images [33] [39].

In terms of psychophysical experiments, "fool-the-reader" evaluations have been proposed [25], [34], [35], aiming to measure the ability of human observers to distinguish simulated phantom images from clinical images. To our knowledge, there are no publications evaluating task-driven phantom texture realism.

A continuous effort is ongoing to improve the realism of mathematical and hybrid phantoms [20], [26]. For the early generation mathematical phantoms, the breast anatomy was defined using empirical but qualitative descriptions of breast anatomy found in the literature [11], [21]–[24]. More recently, mathematical phantom design is often driven by ways to increase statistical realism of simulated phantom images in comparison with clinical images [20], [26]. To our knowledge, no work reports on improvements based on objective and automatic inference of morphological characteristics extracted from clinical fully 3D images, such as from breast CT or MRI reconstructed images. In the field of material science however, objective and automatic inference methods have been successfully applied to describe and simulate heterogeneous structures [40], [41].

In this article, we build upon a previously proposed 3D mathematical breast texture model for small and medium-scale fibroglandular tissue and intra-glandular adipose tissue present in the center part of the breast [25]. The 3D texture model is formulated as two stochastic geometric processes with mathematically tractable characterization. In previous work, the small and medium-scale texture parameters were empirically determined based on visual observations in segmented reconstructed breast CT images. For each of the four simulated BI-RADs breast density classes, simulated breast textures had only a limited morphological variability and the visual realism of simulated images of the breast texture was found to be fair to high [25]. To allow for a larger variability in simulated breast texture morphologies and to increase visual realism, in this work, a method is proposed to objectively and automatically assess the medium-scale parameters from segmented clinical breast CT images. We hypothesized that a set of random ellipsoids exhibiting cluster interaction is representative to model the medium-scale intra-glandular adipose compartments. To reconstruct the ellipsoid set, a multiple birth, death and shift algorithm is proposed. Then, we propose to fit the reconstructed ellipsoid centers to a Matérn cluster process using the minimum contrast estimator. Finally, distributions for the shapes and orientations of the ellipsoids are estimated from reconstructed ellipsoids using maximum likelihood estimators. The feasibility of the method is demonstrated on 16 volumes of interest, extracted from the segmented breast CT images.

To evaluate the realism of our 3D mathematical breast texture model of small and medium-scale fibroglandular tissue and intra-glandular adipose tissue present in the center part of the breast, we analyzed 2D simulated texture projection images in terms of β and LFE and we compared the values to previously published values for clinical images. We also illustrate the visual realism of 2D mammographic projections and 3D reconstructed DBT slices. A more extensive psychophysical "fool-the-reader" experiment was out of scope of this article and was conducted in a previous publication [35].

II. Materials and methods

A. Breast computerized tomography data

To develop the 3D mathematical breast texture model of small and medium-scale fibroglandular and intra-glandular adipose tissues in the center portion of the breast, 3D reconstructed volumes of 16 breasts from 16 patients, acquired with a dedicated breast CT scanner prototype, were used [42]. The selected breast volumes did not contain any identified lesion and they were characterized by a variety of volumetric breast densities. Fig. 1 illustrates a coronal, a sagittal, and a transverse plane of four reconstructed breast CT volumes of predominantly adipose, scattered fibroglandular dense, heterogeneously dense, and extremely dense breasts. First, all volume voxels were classified as either fibroglandular tissue or adipose tissue with a previously developed automatic segmentation algorithm [43], with the same aim of the algorithm by Caballo *et al.* [44]. Next, a cubic volume of interest (VOI) with 3.5 cm

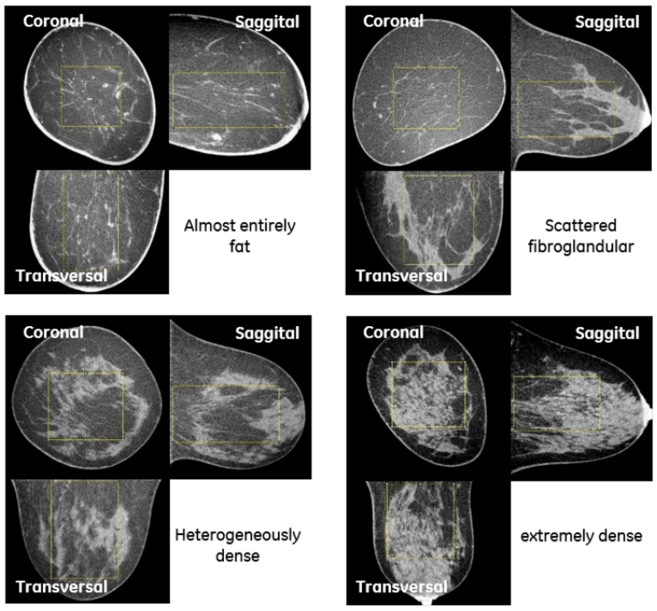

Fig. 1. Illustration of a coronal, a sagittal and a transversal plane from four reconstructed breast CT volumes used in this work to develop the 3D mathematical breast texture model. According to the BI-RADS reporting system, the breast tissues are almost entirely fatty, scattered fibroglandular dense, heterogeneously dense, and extremely dense.

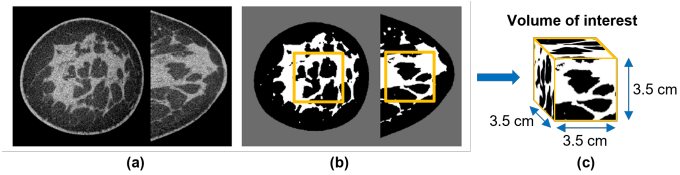

Fig. 2. Illustration of a coronal and sagittal plane from an original (a) and a segmented (b) reconstructed breast CT scan. The yellow lines in (b) indicate the VOI, selected in the central breast tissue region, as input to construct the 3D mathematical breast texture model. The VOI is $3.5\,\text{cm} \times 3.5\,\text{cm} \times 3.5\,\text{cm}$ (c).

TABLE I

SUMMARY OF EXTRACTED AND SEGMENTED VOIS FROM 16 INPUT BREAST CT VOLUMES IN TERMS OF THEIR DIMENSIONS IN NUMBER OF VOXELS, ISOTROPIC VOXEL RESOLUTIONS AND VOLUMETRIC FIBROGLANDULAR DENSITY.

VOI	VOI dimension (number of voxels)	Voxel resolution (mm)	VOI volumetric fibroglandular density (%)
#1	$99 \times 99 \times 99$	0.357	57.2
#2	$99 \times 99 \times 99$	0.354	40.6
#3	$94 \times 94 \times 94$	0.376	25.1
#4	$103 \times 103 \times 103$	0.341	23.5
#5	$103 \times 103 \times 103$	0.343	17.4
#6	$100 \times 100 \times 100$	0.351	37.2
#7	$112 \times 112 \times 112$	0.314	32.9
#8	$96 \times 96 \times 96$	0.366	29.0
#9	$97 \times 97 \times 97$	0.361	25.7
#10	$101 \times 101 \times 101$	0.349	13.9
#11	$128 \times 128 \times 128$	0.275	14.5
#12	$87 \times 87 \times 87$	0.405	09.8
#13	$107 \times 107 \times 107$	0.329	27.1
#14	$87 \times 87 \times 87$	0.405	25.0
#15	$124 \times 124 \times 124$	0.283	20.5
#16	$126 \times 126 \times 126$	0.279	17.2

side length was extracted from the central region of each segmented binary breast CT volume. The distances from the chest wall and breast skin to the nearest VOI boundary were larger than 2 cm, to ensure that the VOI contained mainly fibroglandular and intra-glandular adipose tissue and to avoid the potential presence of subcutaneous and retromammary adipose tissue. The latter is characterized by a different mathematical model. In addition, due to the limited spatial resolution of the segmented breast CT dataset, it would not be possible to well characterize this part of the breast. Fig. 2 shows an original and segmented breast CT reconstructed volume, and a 3D rendering of the extracted cubic VOI. Table I summarizes the characteristics of all 16 extracted and segmented VOIs in terms of the number of voxels, the voxel size and the volumetric fibroglandular density. The volumetric fibroglandular density was computed as the fraction of the voxels containing fibroglandular tissue.

B. 3D breast texture model based on breast CT VOIs

The proposed 3D breast texture model was based on observations from segmented breast CT VOIs. As shown in Fig. 3, we hypothesized that medium-scale intra-glandular adipose tissue compartments can be modeled using a system of overlapping ellipsoids. Also, small scale irregularities observed at the boundaries between the fibroglandular and adipose tissues were modeled using elements of stochastic geometry. An overview of the key steps used to simulate 3D breast texture is shown in Fig. 4.

To model the medium-scale intra-glandular adipose tissue, a *Marked Point Process* (MPP) [45] $\mathbf{Y} = \{\mathbf{\Phi_s}, \boldsymbol{\theta}\}$, of randomly oriented overlapping ellipsoids, defined inside a 3D cube W was proposed (Fig. 4, top). The fibroglandular tissue was defined as the complement of $\mathbf{Y}$. The MPP was characterized by two distributions; $\mathbf{P_s}$, distribution of a *point process* [45] $\mathbf{\Phi_s} = \{x_i, i \in \mathbb{N}\}$, and $\mathbf{P_\theta}$, distribution of a random vector $\boldsymbol{\theta}$. The point process $\mathbf{\Phi_s}$ determines the center points of the ellipsoids, while $\boldsymbol{\theta}$ determines the shapes and orientations of the ellipsoids. More specifically, $\boldsymbol{\theta}$ was set to $(L_a, L_b, L_c, \delta\phi_a, \delta\phi_b, \delta\phi_c)$, where L_a, L_b and L_c are half lengths of the principal axes of the ellipsoids and $\delta\phi_a$, $\delta\phi_b$, $\delta\phi_c$ are three random tilt angles of the ellipsoids around the three principal axes. Each random tilt angle is added to a deterministic rotation angle. The deterministic rotation angles of an ellipsoid are the Euler angles obtained by rotating the ellipsoid, originally aligned with the global coordinate system, to an orientation where its longest principal axis extends to a hypothetical nipple position [46]. A hypothetical nipple position aims to model a texture directionality observed in clinical breast images [47].

To model the small scale irregularities observed at the boundaries of fibroglandular and intra-glandular adipose tissues (Fig. 3), a 3D *Uniform Poisson Point Process* [45] $\mathbf{\Phi_V}$ in the same cube W, defining the centers of a 3D Voronoi tessellation, was proposed (Fig. 4, bottom). The process $\mathbf{\Phi_V}$ was parametrized by a scalar intensity parameter λ_V, controlling the average number of Voronoi

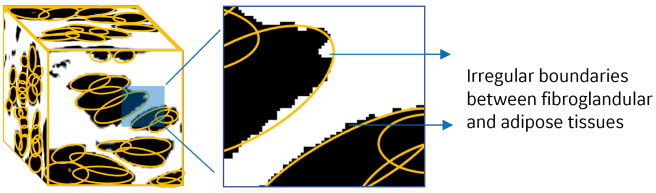

Fig. 3. Illustration of a VOI extracted from a segmented breast CT volume. This figure illustrates that the medium-scale intra-glandular adipose tissue compartments can be well approximated by overlapping ellipsoids (marked in yellow). The small irregularities at the boundaries of fibroglandular and adipose tissues were modeled by boundaries of a 3D Voronoi tessellation.

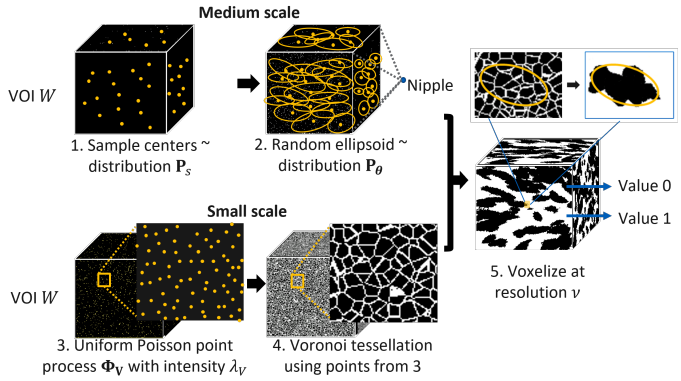

Fig. 4. Overview of the key steps used to create the 3D mathematical breast texture. At one hand, a marked point process is defined serving as the centers of a set of randomly orientated ellipsoids of various sizes. In parallel, a uniform Poisson point process is defined, serving as the basis of 3D Voronoi tessellation. These two process outcomes are combined. To obtain the final texture, Voronoi cells with center inside ellipsoids are turned off.

cells per unit volume [48]. Large values of λ_V give very smooth intra-glandular adipose compartment boundaries while smaller values of λ_V give irregular boundaries. Here, the magnitude of λ_V was chosen to obtain visually similar boundaries as observed in the original breast CT volumes and in simulated mammography images of the segmented breast CT volumes. The λ_V value was set equal to 10 points per mm^3 to obtain 3D Voronoi cells with average sizes equal to 0.1mm^3.

The breast texture model produces discrete 3D volumes in voxelized format as final output. Therefore, a voxelization process combining medium-scale ellipsoids and small scale Voronoi cells was proposed (Fig. 4, right), creating medium-scale fibroglandular and adipose tissues with small irregularities at the boundaries, as observed in breast CT VOIs. The 3D cube W was first discretized into voxelized format at resolution ν, then every voxel was assigned a value of either 0 or 1 depending on its position relative to the small scale Voronoi cells and the medium-scale ellipsoids. More specifically, all voxels belonging to a Voronoi cell were assigned a value of 0, if the center of the Voronoi cell fell inside one of the ellipsoids. All other voxels were assigned a value of 1.

C. Estimating parameters of proposed 3D texture model

The parameters of the medium-scale texture model, *i.e.* the marked point process $\mathbf{Y} = \{\mathbf{\Phi_s}, \boldsymbol{\theta}\}$, were determined with an objective and automatic inference method. We chose to adopt the inference from the reconstruction pipeline proposed by Thiedmann *et al.* [40] since this method allows to reconstruct the individual ellipsoids composing the adipose compartments, that are occult in the segmented breast CT VOIs.

First, a reconstruction step using a dynamic Monte Carlo algorithm was designed to identify the centers, half-axes and orientations of the ellipsoids in each breast CT VOI. Next, statistical analyses were performed to determine the empirical distributions of $\mathbf{\Phi_s}$ and $\boldsymbol{\theta}$. Finally, the parameters of $\mathbf{P_s}$ and $\mathbf{P}_{\boldsymbol{\theta}}$ were estimated. The parameters of $\mathbf{P_s}$ were estimated using a minimum contrast estimator [45], minimizing the squared difference between the theoretical pair correlation function [49] of $\mathbf{\Phi_s}$ and its empirical counterpart measured from the reconstructed ellipsoids. The parameters of $\mathbf{P}_{\boldsymbol{\theta}}$ were estimated using maximum-likelihood method.

1) Reconstruction of ellipsoids from breast CT VOIs: Let $\mathcal{D}$ be a segmented breast CT VOI defined in a 3D cube W, where $\mathcal{D}(x) = 1$ if the voxel x is classified as fibroglandular tissue, and $\mathcal{D}(x) = 0$ if the voxel x is classified as adipose tissue. The reconstruction step, aiming to find the optimal configuration of ellipsoids for $\mathcal{D}$, was formulated as an optimization problem that can be solved using a dynamic Monte Carlo algorithm. The probability density function $f_{\mathbf{Y}}$ of the underlying MPP model $\mathbf{Y}$ was assumed to have a Gibbsian form [50]:

$$f_{\mathbf{Y}}(\mathbf{u}) = \frac{1}{Z_T} \exp\left(-\frac{1}{T} E(\mathbf{u}, \mathcal{D})\right). \quad (1)$$

Here $\mathbf{u} = \{\mathcal{E}_i\}_i$ is a configuration of 3D ellipsoids, where $\forall i$, $\mathcal{E}_i$ is a 3D ellipsoid characterized by its center point x_i and a parameter vector $\boldsymbol{\theta}$ of its shape and orientation, as described in Section II-B. The term $E(\mathbf{u}, \mathcal{D})$ refers to the *energy* and $T \in \mathbb{R}^+$ is a temperature parameter. The term Z_T is a normalization constant that does not need to be computed, since we use a Monte Carlo algorithm that computes only the ratio of probabilities.

The energy term was further decomposed into two parts [51], [52]:

$$E(\mathbf{u}, \mathcal{D}) = \mathcal{L}(\mathbf{u}, \mathcal{D}) + \mathcal{P}(\mathbf{u}). \quad (2)$$

The first part $\mathcal{L}(\mathbf{u}, \mathcal{D})$ is a data fidelity term representing how well a configuration of ellipsoids $\mathbf{u}$ matches the breast CT VOI $\mathcal{D}$. It was formulated as

$$\mathcal{L}(\mathbf{u}, \mathcal{D}) = 1 - \frac{|\{x \in W | \mathcal{D}_{\mathbf{u}}(x) = 0 \text{ and } \mathcal{D}(x) = 0\}|}{|\{x \in W | \mathcal{D}_{\mathbf{u}}(x) = 0 \text{ or } \mathcal{D}(x) = 0\}|}. \quad (3)$$

Here, $|\cdot|$ denotes the number of elements in a set and $\mathcal{D}_{\mathbf{u}}$ is obtained by voxelizing the configuration of ellipsoids $\mathbf{u}$ inside the cube W, that is,

$$\mathcal{D}_{\mathbf{u}}(x) = \begin{cases} 0 & \text{if voxel } x \text{ is inside an ellipsoid of } \mathbf{u}, \\ 1 & \text{otherwise.} \end{cases} \quad (4)$$

The second part $\mathcal{P}(\cdot)$ is a *prior term* containing the a-priori information of the underlying MPP model $\mathbf{Y}$. A model with minimum a-priori information on the distribution of the ellipsoids was chosen and a constraint preventing high overlap ratio between ellipsoids was used to formulate $\mathcal{P}(\mathbf{u})$. That is:

$$\mathcal{P}(\mathbf{u}) = \sum_{\mathcal{E}\in\mathbf{u}} q(\mathcal{E}, \mathbf{u} \setminus \mathcal{E}), \quad (5)$$

with

$$q(\mathcal{E}, \mathbf{u} \setminus \mathcal{E}) = \begin{cases} 0 & \frac{\nu(\mathcal{E}\cap\mathbf{u}\setminus\mathcal{E})}{\nu(\mathcal{E})} \leq 0.95, \\ +\infty & \text{otherwise,} \end{cases} \quad (6)$$

where $\nu(\cdot)$ denotes the continuous 3D volume measure.

Finding the best configuration of ellipsoids $\mathbf{u}^*$ is therefore equivalent to solving the following optimization problem:

$$\mathbf{u}^* = \arg\max_{\mathbf{u}} f_{\mathbf{Y}}(\mathbf{u}) = \arg\min_{\mathbf{u}} \left(\mathcal{L}(\mathbf{u}, \mathcal{D}) + \mathcal{P}(\mathbf{u})\right). \quad (7)$$

Since the analytical solution for (7) is not straightforward, we proposed to use a dynamic *Monte Carlo Markov Chain* algorithm. More specifically, the special case of a multiple birth, death and shift (MBDS) algorithm [52] was adopted, with an iterative procedure aiming to solve equation (7) through stochastically sampling, deleting and modifying multiple ellipsoids. An overview of the key steps of the complete algorithm is described in Fig. 5.

In summary, at each iteration, first a *birth process* occurred, creating multiple random ellipsoids based on some proposal distributions for the ellipsoid centers, half-axis lengths and tilt angles. In this study, a Uniform Poisson point process with intensity parameter γ equal to 0.005 points per mm^3 was used as the proposal process to sample the ellipsoid centers. As of the proposal distributions to sample the half-axis lengths L_a, L_b, L_c and the tilt angles $\delta\phi_a$, $\delta\phi_b$, $\delta\phi_c$ of the ellipsoids, Gaussian and Uniform distributions with parameters empirically determined in our previous study [25] were used. These previously determined proposal distributions allowed to accelerate the convergence of the algorithm, compared to if random probability distributions were used to initialize the algorithm.

After the birth process, each existing ellipsoid was examined with respect to the energy of its current configuration, to determine whether a *death process* or a *shift process* would be performed. More specifically, a probability value $p_d = \frac{r\gamma}{1+r\gamma}$, where

$$r = \exp\left(\frac{E(\mathbf{u}, \mathcal{D}) - E(\mathbf{u} \setminus \mathcal{E}, \mathcal{D})}{T}\right) \quad (8)$$

was first computed representing the potential energy decrease if the death process were to be performed. Then, p_d was compared with a random value v uniformly sampled between 0 and 1. If $p_d > v$, then the death process was performed. Otherwise the shift process was performed. The death process consisted of deleting the examined ellipsoid from the configuration, while the shift process consisted of replacing the examined ellipsoid by a new ellipsoid. The shift process aims to improve the accuracy of covering intra-glandular adipose tissues by ellipsoids, as illustrated in Fig. 6. The shift process was designed in analogy to the Legendre ellipsoid associated with a convex body in classical mechanics [53]. More specifically, for an ellipsoid $\mathcal{E}$ in a configuration $\mathbf{u}$, let $\mathcal{D}_{\mathcal{E}}$ be the binary volume obtained by voxelizing $\mathcal{E}$ inside cube W under the same rule as described in (4). For a segmented breast CT VOI $\mathcal{D}$, we define $K_{\mathcal{E}}(\mathcal{D})$ as

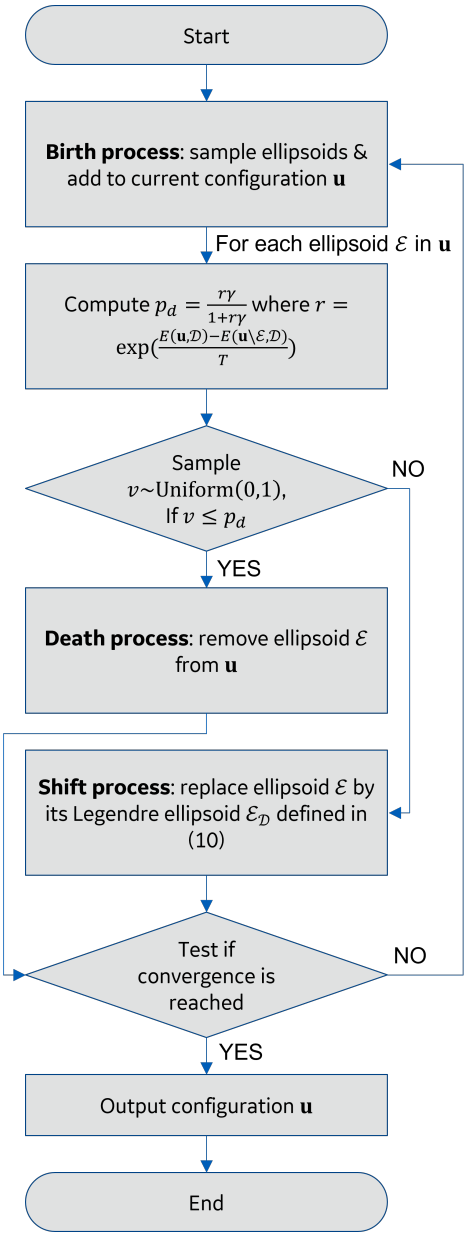

Fig. 5. Steps of the multiple birth, death and shift algorithm.

$$K_{\mathcal{E}}(\mathcal{D}) = \{x \in W | \mathcal{D}(x) = 0 \text{ and } \mathcal{D}_{\mathcal{E}}(x) = 0\}. \quad (9)$$

Then from $K_{\mathcal{E}}(\mathcal{D})$, we define a new ellipsoid $\mathcal{E}_{\mathcal{D}}$ as

$$\mathcal{E}_{\mathcal{D}} = \{y \in \mathbb{R}^3 | (y-\mu)^T \mathbf{\Sigma}^{-1} (y-\mu) \leq 1\}, \quad (10)$$

where

$$\mu = \frac{\sum_{x \in K_{\mathcal{E}}(\mathcal{D})} x}{|K_{\mathcal{E}}(\mathcal{D})|}$$

is the center of mass of $K_{\mathcal{E}}(\mathcal{D})$, and

$$\mathbf{\Sigma} = \frac{\sum_{x \in K_{\mathcal{E}}(\mathcal{D})} 5(x-\mu)(x-\mu)^T}{|K_{\mathcal{E}}(\mathcal{D})|}$$

is a positive-definite real symmetric matrix [53]. The shift of $\mathcal{E}$ consists in replacing $\mathcal{E}$ by the ellipsoid $\mathcal{E}_{\mathcal{D}}$. The idea is that, when $K_{\mathcal{E}}(\mathcal{D})$ is a convex body, $\mathcal{E}_{\mathcal{D}}$ is the unique ellipsoid centered at the center of mass of $K_{\mathcal{E}}(\mathcal{D})$, having the same moment of inertia as $K_{\mathcal{E}}(\mathcal{D})$ about any axis passing through the center of mass [54]. The birth, death and shift processes were repeated until the largest change in the energy values for the 10 most recent iterations did not exceed a pre-defined value ϵ, indicating the convergence of the algorithm. The value of ϵ was set to 0.001 in our study. The algorithm was implemented using the C++ language. To quantify the reconstruction accuracy, the Dice coefficient d was computed for each breast CT VOI $\mathcal{D}$ and its corresponding $\mathcal{D}_{\mathbf{u}}$ obtained from the MBDS algorithm [55], that is

$$d(\mathcal{D}, \mathcal{D}_{\mathbf{u}}) = \frac{2|\{x \in W | \mathcal{D}(x) = 0 \text{ and } \mathcal{D}_{\mathbf{u}}(x) = 0\}|}{|\{x \in W | \mathcal{D}(x) = 0\}| + |\{x \in W | \mathcal{D}_{\mathbf{u}}(x) = 0\}|}.$$

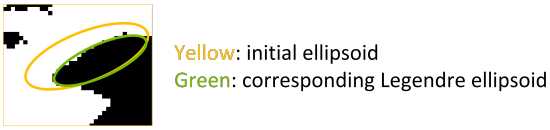

Fig. 6. Illustration of the shift process in the MBDS algorithm. The shift process, which replaces an initial ellipsoid (yellow) by its corresponding Legendre ellipsoid (green), aims to improve the covering accuracy of the intra-glandular tissue.

2) Statistical analyses of reconstructed ellipsoids: After the reconstruction step, empirical statistical analyses were performed for each breast CT VOI to study the distribution $\mathbf{P_s}$ of reconstructed ellipsoid centers, and the distributions $\mathbf{P_\theta}$ of half-axis lengths and random tilt angles.

a) Distribution of reconstructed ellipsoid centers: To analyze the distribution $\mathbf{P_s}$ of the reconstructed ellipsoid centers $\mathbf{\Phi_s}$, the *pair correlation function* (PCF) was estimated for each breast CT VOI. PCF is a second-order statistical descriptor for point processes that is often used to visualize interactions between pairs of points [49]. For a Poisson point process where there is no interaction between any pair of points, the PCF has a constant value of 1. For a point process exhibiting clustering interaction between points, its theoretical PCF is expected to be greater than 1 [49]. For a stationary and isotropic point process, the theoretical PCF, $g(r)$, depends only on the *interpoint distance* $r = \|c_1 - c_2\|$, for any pair of spatial positions c_1 and c_2.

In this study, only small VOIs, measuring 3.5 cm × 3.5 cm × 3.5 cm, were considered. Based on preliminary empirical characterizations [25], we hypothesized that the ellipsoid centers follow a stationary and isotropic point process in such small VOIs. In addition, based on empirical measurements [25], we hypothesized that the ellipsoid centers exhibit a clustering interaction, since overlaps between ellipsoids were observed. To estimate the empirical PCF of the reconstructed ellipsoid centers,the analytical PCF estimator described in [56, p.232] was applied:

$$\hat{g}(r; \Phi_s) = \sum_{p_1, p_2 \in \Phi_s \cap W, p_1 \neq p_2} \frac{\mathbf{k}(\|p_1 - p_2\| - r)}{4\pi r^2 \hat{\lambda}^2 \nu(W_{p_1} \cap W_{p_2})}, \quad (11)$$

where Φ_s is the collection of all ellipsoid centers reconstructed from a breast CT VOI, $\mathbf{k}(\cdot)$ is a smoothing kernel function, $\nu(\cdot)$ is the volume measure, W_{p_1} and W_{p_2} denotes the translation of cube W by points p_1 and p_2 respectively, and $\hat{\lambda}$ is the empirically estimated intensity parameter of Φ_s, expressed as

$$\hat{\lambda} = \frac{|\Phi_s|}{\nu(W)}. \quad (12)$$

The Epanechnikov smoothing kernel [45] was used for $\mathbf{k}(\cdot)$:

$$\mathbf{k}(s) = \begin{cases} \frac{3}{4\delta}(1 - \frac{x^2}{\delta^2}) & \text{if } -\delta \leq s \leq \delta, \\ 0 & \text{otherwise,} \end{cases} \quad (13)$$

for any $s \in \mathbb{R}$, where δ is a bandwidth parameter and was set to $\frac{0.26}{\sqrt[3]{\hat{\lambda}}}$ based on a rule-of-thumb defined in [57].

The estimation of the PCF was performed using the `pcf3est` function implemented in the `R` software package `spatstat` version 1.61 [57] using the default setting.

Next, Poisson envelope tests [58] of the estimated PCFs were performed to check if the reconstructed ellipsoid centers can be modeled as Poisson point process.

b) Distributions of ellipsoid half-axis lengths and random tilt angles: To analyze the distribution of the half-axis lengths L_a, L_b, L_c and tilt angles $\delta\phi_a$, $\delta\phi_b$, $\delta\phi_c$, we assumed them to be independent random variables that were independent from the ellipsoid centers $\mathbf{\Phi_s}$. Histograms of L_a, L_b, L_c, $\delta\phi_a$, $\delta\phi_b$ and $\delta\phi_c$ of the reconstructed ellipsoids were constructed.

3) Estimation of model parameters: Parametric models were proposed to estimate the distributions of the ellipsoid centers, half-axis lengths and random tilt angles. To model the cluster interaction between ellipsoid centers, a three-dimensional *Matérn cluster process* [49] was used and the minimum contrast estimator (MCE) [45] introduced in Section II-C was applied to estimate its parameters. Regarding the half-axis lengths and random tilt angles, Gaussian and Uniform distributions were considered and their parameters were estimated using maximum likelihood estimators.

a) Matérn cluster process for reconstructed ellipsoid centers: A 3D Matérn cluster process $\Phi_{\mathcal{M}}$ is a two-step

stationary and isotropic point process that is entirely determined by three parameters: intensity parameters κ, λ_0, and radius R. To construct a 3D Matérn cluster process, first a set of "parent points" $\{y_i\}_{i\in\mathcal{I}} \subset \mathbb{R}^3$ was sampled from a Uniform Poisson point process with intensity parameter κ. Here $\mathcal{I}$ denotes the set of all indices for the "parent points". For each "parent point" y_i, a sphere with radius R centered at y_i was generated. Then, inside each sphere, a set of "children points" was sampled from another Uniform Poisson point process with intensity parameter λ_0. A realization of the Matérn cluster process was obtained as the collection of all "children points". The MCE method [45] was applied to obtain estimations $\hat{\kappa}$, $\hat{\lambda}_0$, and $\hat{R}$ of respectively κ, λ_0, and R by minimizing the squared difference between the empirical and theoretical PCF. That is,

$$\hat{\kappa}, \hat{\lambda}_0, \hat{R} = \arg\min_{\kappa,\lambda_0,R} \sum_{r\in\mathcal{R}} \left(\hat{g}(r;\Phi_s) - g(r;\kappa,\lambda_0,R)\right)^2, \quad \text{with equality constraint } \hat{\lambda} = \frac{4}{3}\pi\hat{R}^3\hat{\kappa}\hat{\lambda}_0, \tag{14}$$

where $\mathcal{R}$ is a range of interpoint distances for the MCE estimator and was set to vary from 0.2 mm to 30 mm with a step size of 0.2 mm, $\hat{g}(r,\Phi_s)$ is the empirical PCF estimator given in (11), $g(r;\kappa,\lambda_0,R)$ is the theoretical PCF given in [56, p.376]:

$$g(r;\kappa,\lambda_0,R) = \begin{cases} 1 + \frac{3(R-\frac{r}{2})^2(2R+\frac{r}{2})}{8\pi\kappa\lambda_0 R^6} & \text{if } 0 < r \le 2R, \\ 1 & \text{if } r > 2R, \end{cases} \tag{15}$$

and $\hat{\lambda}$ is the empirically estimated intensity parameter given in (12). The equality constraint in (14) was based on the theoretical intensity parameter λ of the the 3D Matérn cluster process [56, p.376]:

$$\lambda = \frac{4}{3}\pi R^3\kappa\lambda_0. \tag{16}$$

The optimization (14) was numerically solved with function `fmincon` implemented in the `Matlab` software (version `2016b`) using the default setting. All optimizations were ran with an initial condition $\kappa = 0.1$, $\lambda_0 = 0.1$ and $R = 1$. Convergence was considered to be reached when the squared difference between the empirical and theoretical PCF was non-decreasing, within a tolerance value of 10^{-6}. Once the 3D Matérn cluster process for each breast CT VOI was estimated, an envelope test [58] was performed to statistically evaluate the Matérn cluster hypothesis.

b) Gaussian and Uniform distributions for ellipsoid half-axis lengths and random tilt angles: Based on histograms of ellipsoid half-axis lengths L_a, L_b, L_c and tilts angles $\delta\phi_a$, $\delta\phi_b$, $\delta\phi_c$, Gaussian distributions were used to model L_a, L_b, L_c, $\delta\phi_b$ and $\delta\phi_c$, while a Uniform distribution was used to model $\delta\phi_a$. Parameters of these distributions were then estimated using maximum likelihood estimators [59]. Kolmogorov-Smirnov tests ($\alpha = 0.05$) of goodness-of-fit [60] were performed to verify the statistical validity of the estimation.

D. Evaluation of simulated texture images

Using the ray-tracing algorithm implemented in CatSim [61], mammographic and DBT projection images were simulated of breast textures generated with the above proposed model. CatSim was configured to model the topology of the GE Healthcare Senographe Pristina mammography system (GE Healthcare, Buc, France). Projection images were created by considering a mono-energetic x-ray spectrum (23 keV) and only quantum noise as noise source. Detector blur was simulated by filtering the presampled images with an empirically assessed convolution kernel. The photon flux was tuned to match the signal-to-noise ratio (SNR) of simulated images with real images acquired under automatic exposure mode. X-ray scatter from the simulated breast texture was not modeled. The photon flux was tuned so that the SNR of simulated projection images matches the SNR for real acquisitions when using automatic exposure conditions. Mechanical breast texture deformation to mimic breast compression during the DBT image acquisition was not modeled. For the visual assessment, the 2D mammography projection images were processed with eContrast3.1 (GE Healthcare's commercial 2D image processing), while for the statistical texture evaluation, no additional processing was applied. DBT projection images were reconstructed using the commercially available ASIR-DBT algorithm for Pristina.

For each investigated VOI from the reconstructed breast CT volumes, 30 breast texture cubes were realized with 50 mm sides and 35 mm thickness using the corresponding set of medium-scale texture parameters estimated in this work. Small-scale Voronoi tessellations were also simulated, with intensity parameter defined in Section II-B. For each simulation condition, the same relative hypothetical nipple position was chosen as in the corresponding breast CT volume, and an isotropic voxel size was set equal to 100 µm.

The power-law index, β, and Laplacian Fractal Entropy (LFE) were used to evaluate the statistical properties of the generated breast textures in 2D mammographic projection images.

β was computed following the method described by Mainprize *et al.* [62]. In summary, the pixel signal intensities in the mammographic projections were converted to log-intensities. Four 256 × 256 regions of interest (ROIs) were extracted from the central, uniform thickness region of the simulated mammographic projections such that adjacent subregions overlapped by 50% in the horizontal and vertical directions. A spatial cosine window function was used to reduce spectral leakage in the power spectrum estimates. The 2D power spectrum was determined for each of the four ROIs and then the average power spectrum for the four ROIs was computed. The power spectral index β was then computed as the inverse of the slope of the linear fit to the log-log plot of the radially averaged power spectrum, as a function of frequency. The 0.15 cycles/mm to 0.7 cycles/mm spatial frequency range was used for the linear fit. These β values were compared

to previously published values for clinical mammography images [62].

LFE was computed following the method described by Abbey *et al.* [33]. A set of 11 Gabor filters was used. Each 2D projection image was converted to log-intensities. Gabor filters spanning 11 center frequencies varying from 0.125 cycles/mm to 4.0 cycles/mm were evaluated at 0°, 30°, 60°, 90°, 130° and 150° orientations. The Gabor filters were sine-phase with a bandwidth of 1.4 octaves and an aspect ratio of 1. Responses were obtained by convolving each Gabor filter with a log-intensity converted projection image. The response histograms were calculated in the 256 × 256 central region of each filtered image and the LFE values were calculated at different frequencies. The histograms binned the central 99% of the responses, with an additional 1% bin for the remaining extreme values. The LFE estimate for a single filter were averaged across the six filter orientations. These LFE values were compared to previously published LFE values for a small set of 20 clinical mammography images [39].

III. Results

A. Estimating parameters of proposed 3D texture model

1) Reconstruction of ellipsoids from breast CT VOIs: Fig. 7 illustrates the convergence of the MBDS algorithm in terms of the energy decrease as a function of the number of iterations for four segmented breast CT VOI (#1, #3, #7 and #11). For these four VOIs, convergence was reached after respectively 6174, 7488, 8172, and 7722 iterations. For the 12 other segmented breast CT VOIs a similar convergence pattern was observed (not shown). For all VOIs, the algorithm was stopped at the 9000^{th} iteration to obtain the final reconstructed sets of ellipsoids. The average runtime for 9000 iterations per breast CT VOI was approximately 20 minutes on a single PC with an Intel(R) Xeon(R) 12-core CPU E5-2630 and 64 Gb memory.

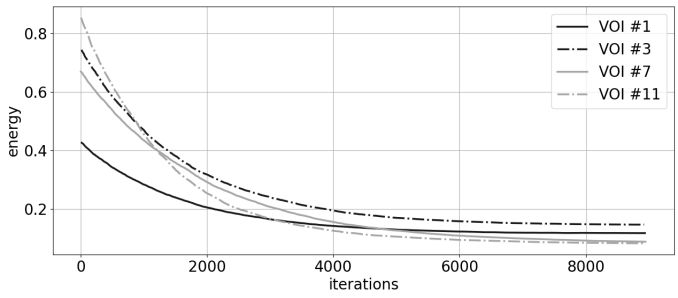

Fig. 7. Illustration of the convergence of the MBDS algorithm in terms of energy defined in (2) as a function of the number of iterations for breast CT VOI #1, #3 #7 and #11. Convergence was reached after about 8000 iterations for all four VOIs.

Fig. 8 illustrates the quality of the final reconstructed sets of ellipsoids in comparison with the input segmented breast CT VOIs #1, #3, #11, and #12. Each set of final reconstructed sets of ellipsoids was discretized into voxelized cubes with the same dimensions and voxel sizes as their corresponding input segmented breast CT VOIs. As a measure for the resemblance of the final reconstructed sets of ellipsoids and input segmented VOIs, Fig. 8 also shows a 2D projection image of each VOI computed by averaging the VOI in the direction perpendicular to the transversal plane. Fig. 8 shows that the distribution and morphology of the medium-scale fibroglandular and intra-glandular adipose tissues in the final reconstructed VOIs agree fairly well with the input segmented breast CT VOIs #1, #3 and #11. Medium scale textures in projection images obtained from final reconstructed sets of ellipsoids and input segmented breast CT VOIs also share fairly similar visual appearance for VOIs #1, #3 and #11. This result was consistent for VOIs #2, #4, #6, #7, #8, #9, #10, #13 and #14 (not shown). However, for VOI #12, the distribution and morphology of the medium-scale fibroglandular and intra-glandular adipose tissues was found to differ greatly in the final reconstructed VOI and the input segmented breast CT VOI. This result was consistent for VOIs #5, #15 and #16 (not shown).

Fig. 9 shows the Dice coefficients [55] computed for all the 16 final reconstructed sets of ellipsoids and input segmented breast CT VOIs. For most of the input VOIs, the Dice coefficient was found to be greater than 65%, indicating fairly good reconstruction quality. There is a tendency that the Dice coefficient increases with increasing VOI volumetric fibroglandular density.

2) Statistical analyses of reconstructed ellipsoids: Fig. 10 compares the empirical PCFs, estimated for the reconstructed ellipsoid centers, and a theoretical Poisson point process for VOI #1, #3, #11, and #12. Fig. 10 also shows the envelopes constructed for the envelope tests allowing to evaluate the goodness of fit of the empirical PCFs with a Poisson point process. For VOI #1, #3 and #11 the empirical PCFs were not completely contained inside the envelope at all interpoint distances. This indicates that a Poisson point process is not a suitable model for the empirical distributions of ellipsoid centers in these VOIs. For VOI #1, #3 and #11 the reconstructed ellipsoid centers also exhibit a clustering effect since the empirical PCF values are greater than 1 for small interpoint distances. This finding confirms our hypothesis that a clustering interaction process describes well the medium-scale intra-glandular adipose compartments. Similar results were obtained for VOI #2, #4, #6, #7, #8, #9, #10, #11, #13 and #14 (not shown).

For VOI #12, the empirical PCF was completely contained within the Poisson envelopes at all interpoint distances and the reconstructed ellipsoid centers do not exhibit a clustering effect, since the empirical PCF values are not greater than 1 at any interpoint distances. Similar results were obtained for VOI #5, #15 and #16 (not shown). For these VOIs, the MBDS algorithm was found to perform many more death operations than shift operations for ellipsoids generated during birth operation. As a consequence, the reconstructed ellipsoid centers were found to be closely related to the initial proposal process used for the birth operation, which was a Poisson point process. These findings indicate that the Poisson point process might be a good candidate to model the empirical

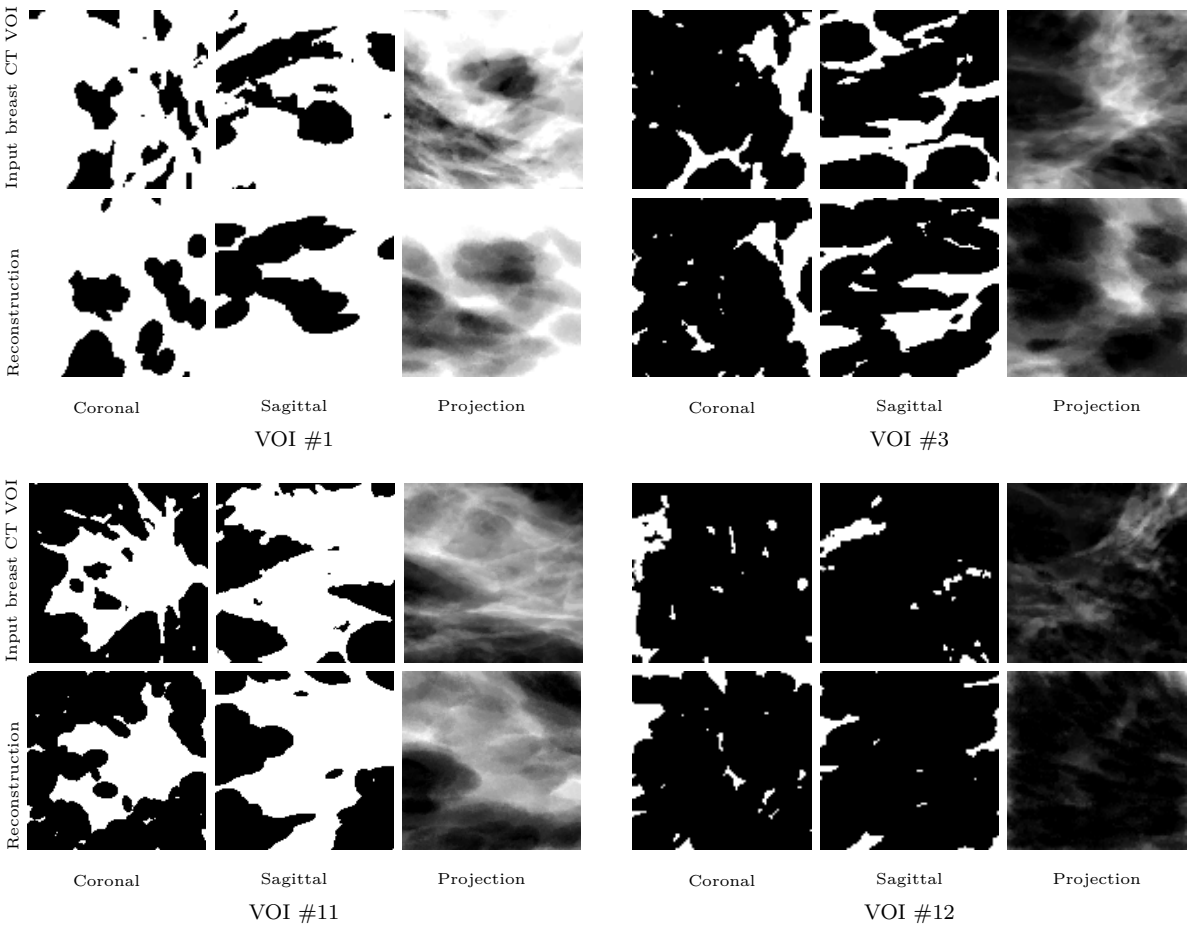

Fig. 8. Coronal slices, sagittal slices and 2D projections of the input segmented breast CT VOIs #1, #3, #11, #12 and corresponding VOIs with reconstructed ellipsoids representing the medium-scale fibroglandular and adipose tissues. The reconstructed ellipsoids were obtained after 9000 iterations of the MBDS algorithm. All images are $3.5\,\mathrm{cm} \times 3.5\,\mathrm{cm}$. Input and reconstructed VOIs have the same spatial resolution. The 2D projections were obtained by averaging the VOIs in the direction perpendicular to the transverse plane. For VOI #1, #3 and #11, the distribution and morphology of the medium-scale fibroglandular and intra-glandular adipose tissues in reconstructed VOIs agree fairly well with the input segmented breast CT VOIs. For VOI #12, the distribution and morphology of the medium-scale fibroglandular and intra-glandular adipose tissues in the reconstructed VOI differ greatly from the original input segmented breast CT VOI.

distributions of the ellipsoid centers in VOI #12, VOI #5, #15 and #16.

For the remainder of the result section, only the 12 VOIs were considered, for which the Poisson point process model of the ellipsoid centers was rejected and for which a clustering interaction of the ellipsoids was observed.

Fig. 11 shows the histograms of the half-axis lengths L_a, L_b, L_c and the tilt angles $\delta\phi_a$, $\delta\phi_b$, $\delta\phi_c$ of the reconstructed ellipsoids for VOI #1, #3, #7 and #11. Based upon a visual assessment, we decided to model the L_a, L_b, L_c, $\delta\phi_b$ and $\delta\phi_c$ distributions as Gaussian distributions and the $\delta\phi_a$ distribution as a Uniform distribution. Similar observations were made for VOI #2, #4, #6, #8, #9, #10, #11, #13 and #14 (not shown).

3) Estimation of model parameters: Fig. 12 shows empirical and theoretical PCFs of the Matérn cluster processes fitted to the ellipsoid centers reconstructed for VOI #1, #3, #7 and #11. Fig. 12 also shows the envelopes constructed for the envelope tests allowing to evaluate the goodness of fit of the empirical PCFs with a Matérn cluster process. At all interpoint distances, the empirical PCFs were completely inside the envelope. This is an indication that the Matérn cluster process can be considered to be a suitable model for describing the spatial arrangement of the ellipsoids, representing the intra-glandular adipose tissue. Similar findings were obtained for the other eight breast CT VOIs (#2, #4, #6, #8, #9, #10, #13 and #14) whereby a clustering interaction was found to be representative to model the medium-scale intra-glandular adipose compartments.

The p-values of the Kolmogorov-Smirnov tests computed to support the hypothesis that L_a, L_b, L_c, $\delta\phi_b$, $\delta\phi_c$ are distributed as Gaussian distributions and that $\delta\phi_a$ are distributed as Uniform distributions are shown under the histograms in Fig. 11. It was found that 21 out 24 p-values are larger than 0.05, indicating strong evidence to retain the null hypotheses and thus that the L_a, L_b, L_c, $\delta\phi_b$, $\delta\phi_c$ are distributed as Gaussian distributions and that $\delta\phi_a$ are distributed as Uniform distributions.

Table II lists the parameters estimated for the 12 VOIs whereby a clustering interaction was found to be representative to model the medium-scale intra-glandular adipose compartments.

TABLE II

ESTIMATED MEDIUM-SCALE MODEL PARAMETERS FROM 12 INPUT VOIS WHEREBY A CLUSTERING INTERACTION WAS FOUND TO BE REPRESENTATIVE TO MODEL THE MEDIUM-SCALE INTRA-GLANDULAR ADIPOSE COMPARTMENTS. HERE $\mathcal{N}(\mu,\sigma)$ DENOTES THE GAUSSIAN DISTRIBUTION WITH MEAN μ, STANDARD DEVIATION σ; AND $\mathcal{U}(l,u)$ DENOTES THE UNIFORM DISTRIBUTION WITH LOWER BOUND l AND UPPER BOUND u.

VOI	κ (points per mm^3)	λ_0 (points per mm^3)	R (mm)	p_{L_a} (mm)	p_{L_b} (mm)	p_{L_c} (mm)	$p_{\delta\phi_a}$ (rad)	$p_{\delta\phi_b}$ (rad)	$p_{\delta\phi_c}$ (rad)
#1	4.24×10^{-3}	2.81×10^{-2}	4.22	$\mathcal{N}(5.48,1.34)$	$\mathcal{N}(2.72,0.55)$	$\mathcal{N}(1.90,0.48)$	$\mathcal{U}(-\frac{\pi}{2},\frac{\pi}{2})$	$\mathcal{N}(-0.05,0.35)$	$\mathcal{N}(-0.04,0.53)$
#2	4.72×10^{-2}	4.33×10^{-2}	1.22	$\mathcal{N}(6.06,1.53)$	$\mathcal{N}(2.79,0.59)$	$\mathcal{N}(2.04,0.52)$	$\mathcal{U}(-\frac{\pi}{2},\frac{\pi}{2})$	$\mathcal{N}((0,0.26)$	$\mathcal{N}(0.01,0.39)$
#3	3.24×10^{-3}	5.98×10^{-3}	5.98	$\mathcal{N}(6.21,1.41)$	$\mathcal{N}(2.77,0.58)$	$\mathcal{N}(2.10,0.57)$	$\mathcal{U}(-\frac{\pi}{2},\frac{\pi}{2})$	$\mathcal{N}(-0.09,0.4)$	$\mathcal{N}(0,0.26)$
#4	1.01×10^{-4}	1.52×10^{-2}	10.41	$\mathcal{N}(5.98,1.42)$	$\mathcal{N}(2.82,0.56)$	$\mathcal{N}(2.06,0.53)$	$\mathcal{U}(-\frac{\pi}{2},\frac{\pi}{2})$	$\mathcal{N}(-0.23,0.43)$	$\mathcal{N}(0.04,0.51)$
#6	5.65×10^{-4}	1.19×10^{-2}	6.98	$\mathcal{N}(5.93,1.47)$	$\mathcal{N}(2.81,0.58)$	$\mathcal{N}(2.04,0.52)$	$\mathcal{U}(-\frac{\pi}{2},\frac{\pi}{2})$	$\mathcal{N}(-0.38,0.53)$	$\mathcal{N}(-0.01,0.47)$
#7	2.87×10^{-4}	1.92×10^{-2}	5.82	$\mathcal{N}(5.88,1.44)$	$\mathcal{N}(2.75,0.56)$	$\mathcal{N}(2.03,0.52)$	$\mathcal{U}(-\frac{\pi}{2},\frac{\pi}{2})$	$\mathcal{N}(-0.15,0.38)$	$\mathcal{N}(0.01,0.5)$
#8	1.10×10^{-3}	1.79×10^{-2}	5.15	$\mathcal{N}(5.87,1.45)$	$\mathcal{N}(2.74,0.59)$	$\mathcal{N}(2.04,0.53)$	$\mathcal{U}(-\frac{\pi}{2},\frac{\pi}{2})$	$\mathcal{N}(-0.19,0.51)$	$\mathcal{N}(0,0.47)$
#9	1.75×10^{-3}	1.84×10^{-2}	4.47	$\mathcal{N}(6.11,1.49)$	$\mathcal{N}(2.80,0.57)$	$\mathcal{N}(2.10,0.53)$	$\mathcal{U}(-\frac{\pi}{2},\frac{\pi}{2})$	$\mathcal{N}(-0.15,0.43)$	$\mathcal{N}(0.02,0.49)$
#10	1.37×10^{-2}	6.43×10^{-3}	3.64	$\mathcal{N}(6.17,1.44)$	$\mathcal{N}(2.85,0.58)$	$\mathcal{N}(2.12,0.54)$	$\mathcal{U}(-\frac{\pi}{2},\frac{\pi}{2})$	$\mathcal{N}(-0.18,0.47)$	$\mathcal{N}(-0.02,0.45)$
#11	3.41×10^{-3}	3.09×10^{-2}	3.85	$\mathcal{N}(6.06,1.39)$	$\mathcal{N}(2.79,0.56)$	$\mathcal{N}(2.10,0.54)$	$\mathcal{U}(-\frac{\pi}{2},\frac{\pi}{2})$	$\mathcal{N}(-0.28,0.47)$	$\mathcal{N}(-0.01,0.43)$
#13	8.21×10^{-4}	1.38×10^{-2}	6.61	$\mathcal{N}(5.97,1.36)$	$\mathcal{N}(2.78,0.58)$	$\mathcal{N}(2.04,0.53)$	$\mathcal{U}(-\frac{\pi}{2},\frac{\pi}{2})$	$\mathcal{N}(-0.15,0.43)$	$\mathcal{N}(0.03,0.48)$
#14	6.64×10^{-4}	5.72×10^{-3}	9.99	$\mathcal{N}(6.19,1.47)$	$\mathcal{N}(2.79,0.61)$	$\mathcal{N}(2.18,0.59)$	$\mathcal{U}(-\frac{\pi}{2},\frac{\pi}{2})$	$\mathcal{N}(0,0.26)$	$\mathcal{N}(-0.01,0.38)$

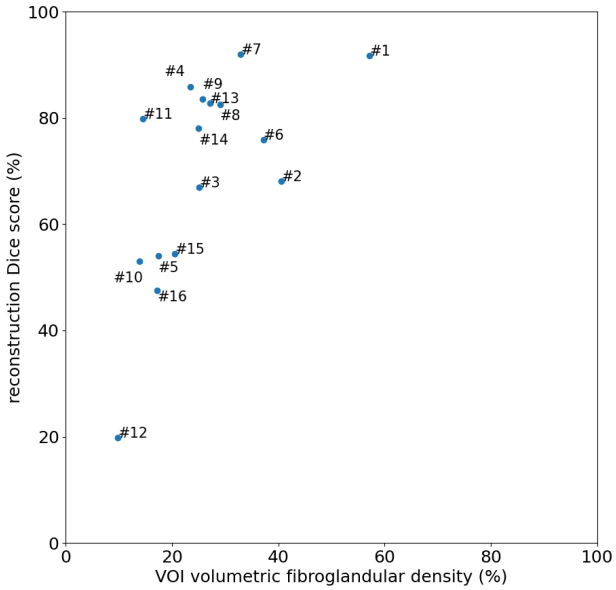

Fig. 9. Dice coefficients for all 16 reconstructed sets of ellipsoids and input segmented breast CT VOIs, as a function of VOI volumetric fibroglandular density. For the majority of the input VOIs, the Dice coefficients were found to be greater than 65%, indicating fairly good reconstruction quality. There is a tendency that the dice coefficient tends increases with increasing volumetric fibroglandular VOI density.

B. Evaluation of simulated texture images

1) Visual image texture evaluation: Fig. 13 gives examples of 2D mammographic projection images and DBT reconstructed slices simulated from the texture volumes generated using the method proposed in this article. Radiologists reported that these images were highly realistic in comparison with clinical images. For a more profound psychophysical evaluation on the visual realism of simulated images from our texture volumes, we refer to our previously published article [35]. The simulated texture images were found to have an increased morphological variety compared to texture images generated from our previous model [25].

2) Statistical image texture evaluation: Fig. 14 shows an example power spectrum plotted versus spatial frequency on a log-log scale and the corresponding linear fit used to estimate β. From a comparison of several cases, a fit with an upper limit of 0.7 cycles/mm was found to lie just inside the "linear" inverse power-law region. Therefore, the linear regression of the power spectrum was calculated across a frequency interval [0.15 cycles/mm, 0.7 cycles/mm] to determine values of the power-law exponent β. Table III shows the power-law exponents β for the simulated mammographic projections of the 30 texture realizations generated for each of the 12 sets of model parameters. For the ensemble of all texture types, β was found to range from 3.5 to 4.4 while β was found to vary from 2.3 to 3.6 for the 2686 mammograms previously analyzed by Mainprize *et al.* [62]. Note that Mainprize *et al.* limited the fit to extract β from the mammography power spectra to between 0.15 cycles/mm and 1.0 cycles/mm. Mainprize *et al.* showed a small decrease in β when the maximum of the frequency range was varied from 0.7 cycles/mm to 1.0 cycles/mm. Therefore, we believe it is justified to compare the results from both studies.

Fig. 15 shows the LFE results determined for the simulated mammographic projections of the 30 texture realizations generated for each of the 12 sets of model parameters as well as the previously reported LFE of a set of 20 mammograms [39]. There is a general agreement in the LFE results of the simulated textures and the clinical mammograms.

IV. DISCUSSION AND CONCLUSION

This work describes a method to mathematically model small and medium-scale fibroglandular and intra-glandular adipose tissues present in the center part of the breast. The method builds upon a previously proposed 3D solid

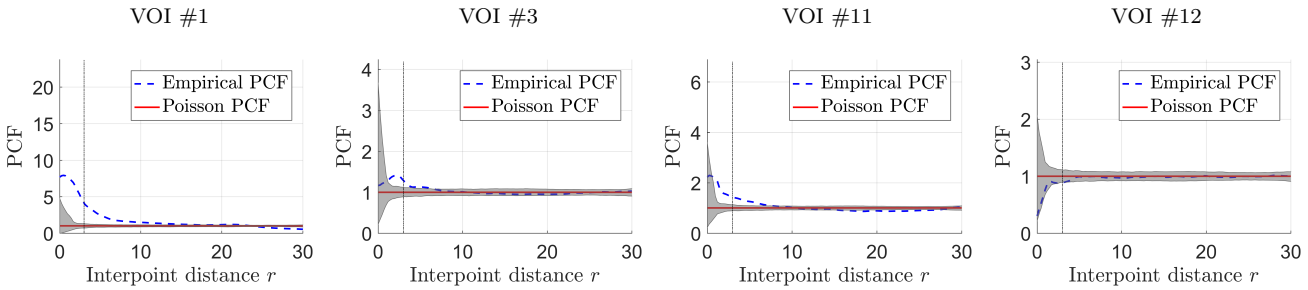

Fig. 10. Comparison of the empirical PCFs, estimated from the reconstructed ellipsoid centers, and the theoretical Poisson PCFs for VOI #1, #3, #11 and #12. For VOI #1, #3 and #11, the empirical PCFs are not completely contained within the Poisson envelopes (gray surfaces) indicating that a Poisson point process is not a suitable candidate to model the distributions of ellipsoid centers in these VOIs. For VOI #1, #3 and #11, PCF values larger than one for small interpoint distances indicate clustering interaction between reconstructed ellipsoid centers. For VOI #12, the empirical PCF of reconstructed ellipsoid centers is completely contained within the Poisson envelopes, indicating that a Poisson point process is a good candidate to model the distribution of ellipsoid centers. For VOI #12, PCF values are not larger than one for any interpoint distance, indicating no clustering interaction between reconstructed ellipsoid centers.

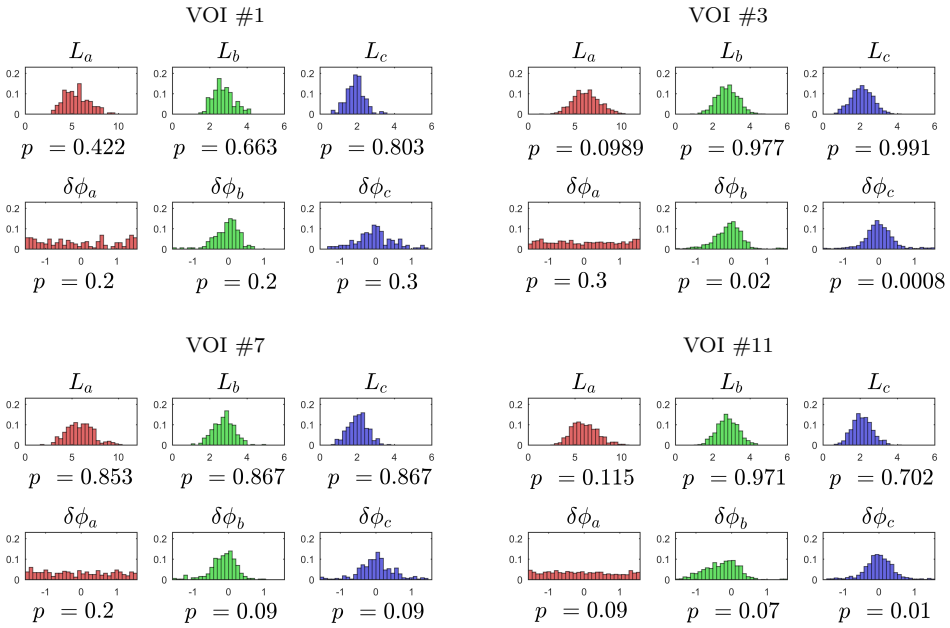

Fig. 11. Histograms of the half-axis lengths $\boldsymbol{L_a}$, $\boldsymbol{L_b}$, $\boldsymbol{L_c}$ and the tilt angles $\boldsymbol{\delta\phi_a}$, $\boldsymbol{\delta\phi_b}$, $\boldsymbol{\delta\phi_c}$ of reconstructed ellipsoids for VOI #1, #3, #7 and #11. Visual observations indicate that $\boldsymbol{L_a}$, $\boldsymbol{L_b}$, $\boldsymbol{L_c}$, $\boldsymbol{\delta\phi_b}$ and $\boldsymbol{\delta\phi_c}$ can be modeled as Gaussian distributions and $\boldsymbol{\delta\phi_a}$ can be modeled as a Uniform distribution. Numbers under the histograms indicate $\boldsymbol{p}$-values of Kolmogorov-Smirnov tests, with estimated Gaussian distributions as null-hypotheses for $\boldsymbol{L_a}$, $\boldsymbol{L_b}$, $\boldsymbol{L_c}$, $\boldsymbol{\delta\phi_b}$, $\boldsymbol{\delta\phi_c}$ and estimated Uniform distribution for $\boldsymbol{\delta\phi_a}$. These $\boldsymbol{p}$-value indicate that the estimated distributions provide statistically good fit to the histograms.

breast texture model formulated as stochastic geometric processes with mathematically tractable characterization [25]. In this work, we objectively infer the medium-scale parameters from segmented clinical breast CT images. Compared to our previous model, whereby simulation parameters were based upon empirical observations, the here proposed inference method substantially augmented the ability to generate textures with larger morphological variety.

The average β values from simulated texture images (3.7 to 4.2) of the 12 different VOIs are higher than the average β value from 2D clinical images (2.87). We attribute the higher β values to the lack of finer anatomical components such as blood vessels, Cooper's ligaments and other fibers, which are depicted as higher frequencies in images. These higher frequency components tend to increase the magnitude of the power spectra towards the upper frequency limit, thus reducing the slope β. Additionally, the breast texture was not deformed so as to mimic breast compression in breast x-ray imaging exams, which may cause different image texture appearance and thus shifts in β values. Finally, the thickness of the phantom may impact the magnitude of the β values; only 3.5cm thick texture cubes were considered, while the compressed thicknesses of the real breasts in the article by [62] very likely span a range of typically clinical values.

On the other hand, the 2D simulated mammographic images of the 3D breast texture model and clinical mammography images have similar LFE. At the lower frequencies, due to the lack of finer anatomical details, the

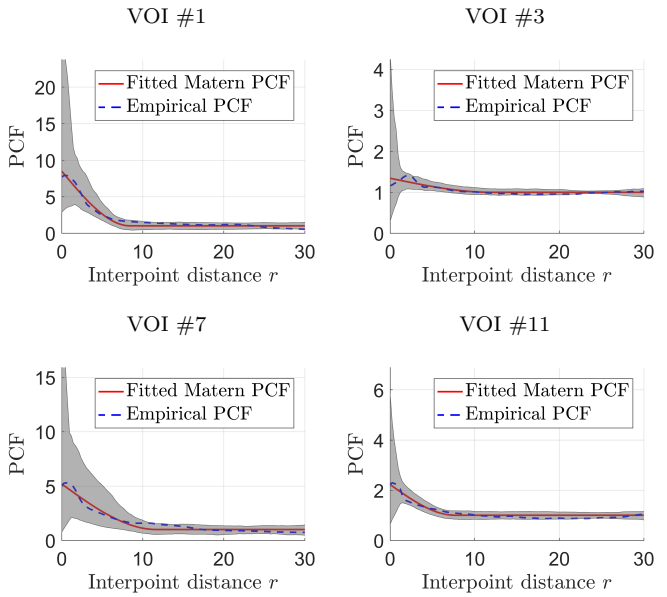

Fig. 12. Comparison of the empirical PCFs and the theoretical PCFs of the Matérn cluster processes fitted to ellipsoid centers reconstructed from VOI #1, #3, #7 and #11. The empirical PCFs fall inside the PCF envelopes (gray surfaces) at all interpoint distances, indicating good fits.

TABLE III
POWER LAW SPECTRAL INDEX β VALUES COMPUTED ON MAMMOGRAPHIC PROJECTIONS SIMULATED USING MODELS WITH PARAMETERS ESTIMATED FROM 12 VOIS. MEAN AND STANDARD DEVIATION VALUES WERE MEASURED ON 30 RANDOM SIMULATIONS PER VOI.

Parameter set	β **value**
VOI #1	4.14 ± 0.11
VOI #2	3.81 ± 0.12
VOI #3	3.79 ± 0.15
VOI #4	4.12 ± 0.17
VOI #6	4.14 ± 0.12
VOI #7	4.15 ± 0.12
VOI #8	4.10 ± 0.17
VOI #9	4.07 ± 0.13
VOI #10	3.71 ± 0.14
VOI #11	3.93 ± 0.15
VOI #13	4.06 ± 0.15
VOI #14	3.94 ± 0.12

simulated texture images are characterized by higher LFE values than the clinical images. We believe that this is due to the presence of regions of nearly uniform signal intensities which increase the response histograms at lower frequencies.

While this study shows that the phantom texture images have higher second-order statistical properties compared to clinical images, a previous psychophysical "fool-the-reader" experiment performed on FFDM and DBT images with radiologists showed that the simulated phantom texture images have high visual resemblance with clinical images [35]. This result confirms that psychophysical experiments with radiologists have an added value in optimizing phantom realism. More work is needed to understand the phantom realism for task-based assessments such as lesion detection and characterization tasks. In order to be effective for evaluating the performance of breast x-ray imaging applications, further validation is required depending on its intended use.

The proposed method can be applied in any mathematical phantom model simulating medium-scale fibroglandular tissue and intra-glandular adipose tissue present in the center part of the breast. Similarly to other mathematical phantom models, the proposed texture model has the advantage that it provides the user with a large number of independent random texture samples, in a controlled and reproducible environment. After execution of a large VCT, the texture phantoms do not need to be stored as such; knowledge of the random seeds and parameter settings used to create the textured phantoms allow to recreate the same phantoms.

We believe that the proposed method, to first infer 3D model parameters from 3D breast CT volumes and then to generate a 3D virtual breast texture model, may serve as an example for modeling different anatomical body parts. The model details require consideration on a case-by-case basis. The proposed method needs a fully 3D image datasets of the target anatomy part so that tissue types can be distinguished from each other in a straightforward manner and classified accordingly. We believe that it would be very difficult to apply the proposed inference approach to either projection images or pseudo-3D clinical datasets since the gray level distributions from the various anatomical parts can not be easily distinguished from each other due to tissue type superimposition.

The proposed method has several opportunities for further improvement.

First, the limited spatial resolution and high image noise of the reconstructed breast CT volume dataset used as input for our texture model, may lead to intrinsic inaccuracies in the classification of the underlying adipose and fibroglandular tissues.

Secondly, the performance of the reconstruction step could be further investigated in a more theoretical and quantitative fashion. Among the 16 extracted segmented breast CT VOIs, the 12 segmented VOIs with higher fibroglandular density satisfied our underlying hypothesis that a clustering interaction process describes well the medium-scale intra-glandular adipose compartments. The 4 segmented VOIs with lower fibroglandular density did not exhibit a clustering interaction and require a different, to be defined, underlying mathematical model. In a future study, theoretical quantification of the reconstruction performance as a function of the volumetric breast density could be investigated.

Thirdly, to reduce the optimization complexity in the inference step, the distributions of the ellipsoid half-axis lengths and the ellipsoid centers were independently estimated. This may be a simplification of a more complex repartitioning of intra-glandular adipose compartments in real breasts. The correlation between the half-axis lengths

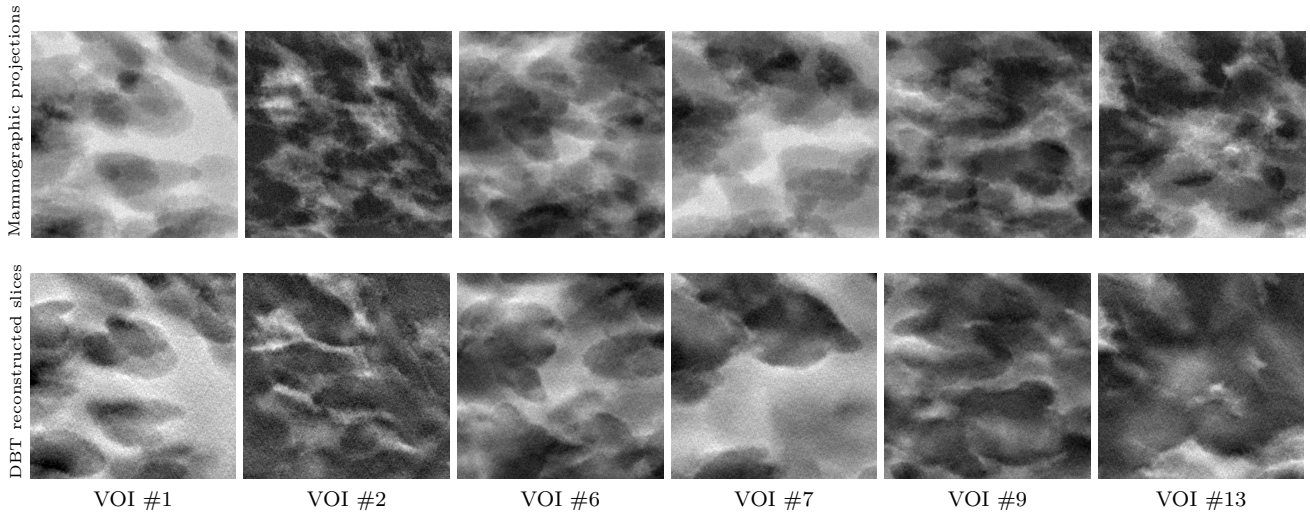

Fig. 13. Examples of 2D mammographic projection images (top) and DBT reconstructed slices (bottom) simulated from the texture volumes generated using parameter sets derived from VOI #1, #2, #6, #7, #9 and #13. All images are $3.5\,\mathrm{cm} \times 3.5\,\mathrm{cm}$. Simulated texture images have an increased morphological variety compared to texture images generated from our previous model [25].

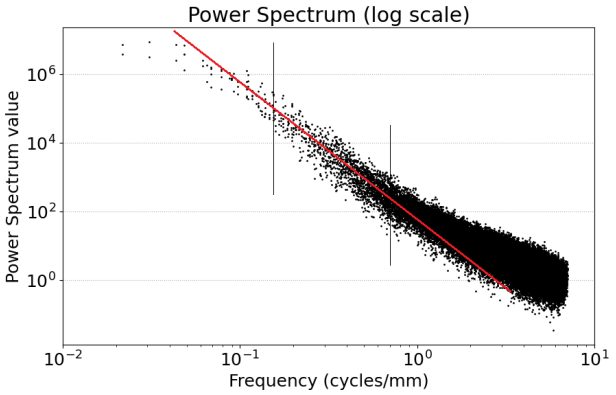

Fig. 14. Power spectrum profile of a simulated 2D texture image. The linear regression of the power spectrum was calculated across a frequency interval [0.15 cycles/mm, 0.7 cycles/mm] to determine values of the power-law exponent β.

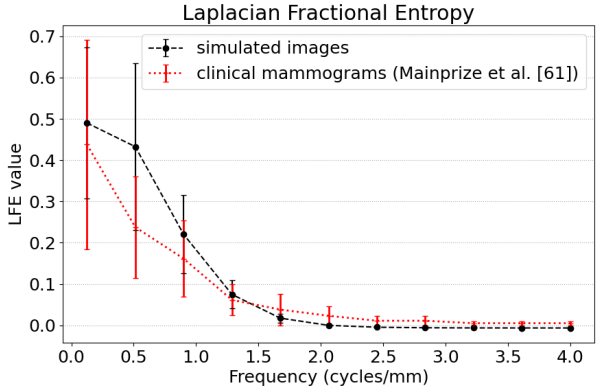

Fig. 15. LFE (mean and standard deviation) computed from 30 2D simulated texture images for each of the 12 model parameters. The LFE data for the clinical mammography images are shown for reference [39]. The average LFE values from the simulated texture images are in close agreement with the reference clinical data across all frequencies.

and the centers of the ellipsoids could be further investigated by studying the mark correlation function of the reconstructed ellipsoids.

Fourthly, as mentioned above, the absence of texture deformation, mimicking breast compression, may impact the texture realism in simulated images. Therefore, the simulated texture cubes could be deformed using a state-of-the-art biomechanical breast model or a mathematical model allowing to geometrically deform the texture cubes. Next, the deformed texture could be evaluated in terms of statistical image realism (β & LFE) and visual image realism. A major limitation of this exercise however is the realism of the deformation since the texture block does not include a chest-wall and ligaments, present in a real breast, which introduce constraints to the biomechanical deformation process.

Finally, 12 sets of model parameters were obtained from breast CT images of 12 different women. To further augment morphological variability of simulated texture realizations, the here proposed method could be applied to a larger number of breast CT datasets from different women. In a future study, it might be interesting to analyze how the model parameters vary with respect to BI-RADS breast density categories and breast texture descriptors, allowing to create a unified model.

Acknowledgment

The authors would like to thank Prof. John Boone from UCDavis for kindly providing the clinical breast CT datasets.

References

[1] N. V. Ruiter, C. Zhang, P. R. Bakic, A.-K. Carton, J. Kuo, and A. D. Maidment, "Simulation of tomosynthesis images based on an anthropomorphic software breast tissue phantom," in *Medical Imaging 2008: Visualization, Image-Guided Procedures, and Modeling*, vol. 6918, p. 69182I, International Society for Optics and Photonics, 2008.

[2] P. R. Bakic, C. Li, E. West, M. Sak, S. C. Gavenonis, N. Duric, and A. D. Maidment, "Comparison of 3d and 2d breast density estimation from synthetic ultrasound tomography images and digital mammograms of anthropomorphic software breast phantoms," in *Medical Imaging 2011: Physics of Medical Imaging*, vol. 7961, p. 79610Z, International Society for Optics and Photonics, 2011.

[3] R. Zeng, S. Park, P. Bakic, and K. J. Myers, "Evaluating the sensitivity of the optimization of acquisition geometry to the choice of reconstruction algorithm in digital breast tomosynthesis through a simulation study," *Physics in Medicine & Biology*, vol. 60, no. 3, p. 1259, 2015.

[4] A. Badano, C. G. Graff, A. Badal, D. Sharma, R. Zeng, F. W. Samuelson, S. J. Glick, and K. J. Myers, "Evaluation of digital breast tomosynthesis as replacement of full-field digital mammography using an in silico imaging trial," *JAMA network open*, vol. 1, no. 7, pp. e185474–e185474, 2018.

[5] P. R. Bakic, B. Barufaldi, D. Higginbotham, S. P. Weinstein, A. N. Avanaki, K. S. Espig, A. Xthona, T. R. Kimpe, and A. D. Maidment, "Virtual clinical trial of lesion detection in digital mammography and digital breast tomosynthesis," in *Medical Imaging 2018: Physics of Medical Imaging*, vol. 10573, p. 1057306, International Society for Optics and Photonics, 2018.

[6] R. S. de la Rosa, A.-K. Carton, P. M. de Carvalho, I. Bloch, and S. Muller, "Analysis of CEDBT and CESM performance using a realistic x-ray simulation platform," in *2019 IEEE 16th International Symposium on Biomedical Imaging (ISBI 2019)*, pp. 1070–1073, IEEE, 2019.

[7] S. J. Glick and L. C. Ikejimba, "Advances in digital and physical anthropomorphic breast phantoms for x-ray imaging," *Medical physics*, vol. 45, no. 10, pp. e870–e885, 2018.

[8] C. M. Li, W. P. Segars, G. D. Tourassi, J. M. Boone, and J. T. Dobbins, "Methodology for generating a 3D computerized breast phantom from empirical data," *Medical physics*, vol. 36, no. 7, pp. 3122–3131, 2009.

[9] N. Kiarashi, J. Y. Lo, Y. Lin, L. C. Ikejimba, S. V. Ghate, L. W. Nolte, J. T. Dobbins, W. P. Segars, and E. Samei, "Development and application of a suite of 4-d virtual breast phantoms for optimization and evaluation of breast imaging systems," *IEEE transactions on medical imaging*, vol. 33, no. 7, pp. 1401–1409, 2014.

[10] A. Sarno, G. Mettivier, F. di Franco, A. Varallo, K. Bliznakova, A. M. Hernandez, J. M. Boone, and P. Russo, "Dataset of patient-derived digital breast phantoms for in silico studies in breast computed tomography, digital breast tomosynthesis, and digital mammography," *Medical Physics*, vol. 48, no. 5, pp. 2682–2693, 2021.

[11] P. R. Bakic, M. Albert, D. Brzakovic, and A. D. Maidment, "Mammogram synthesis using a 3d simulation. i. breast tissue model and image acquisition simulation," *Medical physics*, vol. 29, no. 9, pp. 2131–2139, 2002.

[12] P. R. Bakic, M. Albert, D. Brzakovic, and A. D. Maidment, "Mammogram synthesis using a 3d simulation. ii. evaluation of synthetic mammogram texture," *Medical physics*, vol. 29, no. 9, pp. 2140–2151, 2002.

[13] P. R. Bakic, M. Albert, D. Brzakovic, and A. D. Maidment, "Mammogram synthesis using a three-dimensional simulation. iii. modeling and evaluation of the breast ductal network," *Medical Physics*, vol. 30, no. 7, pp. 1914–1925, 2003.

[14] P. R. Bakic, C. Zhang, and A. D. Maidment, "Development and characterization of an anthropomorphic breast software phantom based upon region-growing algorithm," *Medical physics*, vol. 38, no. 6Part1, pp. 3165–3176, 2011.

[15] F. Chen, P. R. Bakic, A. D. Maidment, S. T. Jensen, X. Shi, and D. D. Pokrajac, "Description and characterization of a novel method for partial volume simulation in software breast phantoms," *IEEE transactions on medical imaging*, vol. 34, no. 10, pp. 2146–2161, 2015.

[16] D. D. Pokrajac, A. D. Maidment, and P. R. Bakic, "Optimized generation of high resolution breast anthropomorphic software phantoms," *Medical physics*, vol. 39, no. 4, pp. 2290–2302, 2012.

[17] C. K. Abbey, P. R. Bakic, D. D. Pokrajac, A. D. Maidment, M. P. Eckstein, and J. M. Boone, "Non-gaussian statistical properties of virtual breast phantoms," in *Medical Imaging 2014: Image Perception, Observer Performance, and Technology Assessment*, vol. 9037, pp. 100–107, SPIE, 2014.

[18] P. R. Bakic, D. D. Pokrajac, and A. D. Maidment, "Computer simulation of the breast subcutaneous and retromammary tissue for use in virtual clinical trials," in *Medical Imaging 2017: Physics of Medical Imaging*, vol. 10132, p. 101325C, International Society for Optics and Photonics, 2017.

[19] B. A. Lau, I. Reiser, R. M. Nishikawa, and P. R. Bakic, "A statistically defined anthropomorphic software breast phantom," *Medical physics*, vol. 39, no. 6Part1, pp. 3375–3385, 2012.

[20] B. Barufaldi, C. K. Abbey, M. A. Lago, T. L. Vent, R. J. Acciavatti, P. R. Bakic, and A. D. Maidment, "Computational breast anatomy simulation using multi-scale perlin noise," *IEEE Transactions on Medical Imaging*, vol. 40, no. 12, pp. 3436–3445, 2021.

[21] D. M. Mahr, R. Bhargava, and M. F. Insana, "Three-dimensional in silico breast phantoms for multimodal image simulations," *IEEE transactions on medical imaging*, vol. 31, no. 3, pp. 689–697, 2012.

[22] K. Bliznakova, Z. Bliznakov, V. Bravou, Z. Kolitsi, and N. Pallikarakis, "A three-dimensional breast software phantom for mammography simulation," *Physics in Medicine & Biology*, vol. 48, no. 22, p. 3699, 2003.

[23] C. G. Graff, "A new open-source multi-modality digital breast phantom," in *SPIE Medical Imaging*, pp. 978309–978309, International Society for Optics and Photonics, 2016.

[24] A.-K. Carton, A. Grisey, P. M. de Carvalho, C. Dromain, and S. Muller, "A virtual human breast phantom using surface meshes and geometric internal structures," in *International Workshop on Digital Mammography*, pp. 356–363, Springer, 2014.

[25] Z. Li, A. Desolneux, S. Muller, and A.-K. Carton, "A novel 3D stochastic solid breast texture model for x-ray breast imaging," in *International Workshop on Digital Mammography*, pp. 660–667, Springer, 2016.

[26] X. Chen, X. Gong, C. G. Graff, M. Santana, G. M. Sturgeon, T. J. Sauer, R. Zeng, S. J. Glick, and J. Y. Lo, "High-resolution, anthropomorphic, computational breast phantom: fusion of rule-based structures with patient-based anatomy," in *Medical Imaging 2017: Physics of Medical Imaging*, vol. 10132, pp. 464–469, SPIE, 2017.

[27] F. O. Bochud, C. K. Abbey, and M. P. Eckstein, "Statistical texture synthesis of mammographic images with clustered lumpy backgrounds," *Optics express*, vol. 4, no. 1, pp. 33–43, 1999.

[28] C. Castella, K. Kinkel, F. Descombes, M. P. Eckstein, P.-E. Sottas, F. R. Verdun, and F. O. Bochud, "Mammographic texture synthesis: second-generation clustered lumpy backgrounds using a genetic algorithm," *Optics express*, vol. 16, no. 11, pp. 7595–7607, 2008.

[29] M. A. Kupinski, E. Clarkson, J. W. Hoppin, L. Chen, and H. H. Barrett, "Experimental determination of object statistics from noisy images," *JOSA A*, vol. 20, no. 3, pp. 421–429, 2003.

[30] H. Liang, S. Park, B. D. Gallas, K. J. Myers, and A. Badano, "Image browsing in slow medical liquid crystal displays," *Academic Radiology*, vol. 15, no. 3, pp. 370–382, 2008.

[31] A. E. Burgess, F. L. Jacobson, and P. F. Judy, "Human observer detection experiments with mammograms and power-law noise," *Medical physics*, vol. 28, no. 4, pp. 419–437, 2001.

[32] L. Cockmartin, H. Bosmans, and N. Marshall, "Comparative power law analysis of structured breast phantom and patient images in digital mammography and breast tomosynthesis," *Medical physics*, vol. 40, no. 8, p. 081920, 2013.

[33] C. K. Abbey, P. R. Bakic, D. D. Pokrajac, A. D. Maidment, M. P. Eckstein, and J. M. Boone, "Evaluation of non-gaussian statistical properties in virtual breast phantoms," *Journal of Medical Imaging*, vol. 6, no. 2, p. 025502, 2019.

[34] A.-K. Carton, P. M. de Carvalho, Z. Li, C. Dromain, and S. Muller, "Assessment of mass detection performance in contrast enhanced digital mammography," in *Medical Imaging 2015: Image Perception, Observer Performance, and Technology Assessment*, vol. 9416, pp. 36–44, SPIE, 2015.

[35] S. Marinov, A.-K. Carton, L. Cockmartin, N. W. Marshall, C. Van Ongeval, R. S. De la Rosa, S. Muller, and H. Bosmans, "Evaluation of the visual realism of breast texture phantoms in digital mammography," in *15th International Workshop on Breast Imaging (IWBI2020)*, vol. 11513, p. 1151314, International Society for Optics and Photonics, 2020.

[36] J. J. Heine, S. R. Deans, D. K. Cullers, R. Stauduhar, and L. P. Clarke, "Multiresolution statistical analysis of high-resolution

digital mammograms," *IEEE Transactions on medical imaging*, vol. 16, no. 5, pp. 503–515, 1997.
[37] E. Engstrom, I. Reiser, and R. Nishikawa, "Comparison of power spectra for tomosynthesis projections and reconstructed images," *Medical physics*, vol. 36, no. 5, pp. 1753–1758, 2009.
[38] K. G. Metheany, C. K. Abbey, N. Packard, and J. M. Boone, "Characterizing anatomical variability in breast ct images," *Medical physics*, vol. 35, no. 10, pp. 4685–4694, 2008.
[39] J. G. Mainprize, G. E. Mawdsley, A.-K. Carton, Z. Li, R. Klausz, S. Muller, and M. J. Yaffe, "Full-size anthropomorphic phantom for 2D and 3D breast x-ray imaging," in *15th International Workshop on Breast Imaging (IWBI2020)*, vol. 11513, p. 1151302, International Society for Optics and Photonics, 2020.
[40] R. Thiedmann, O. Stenzel, A. Spettl, P. R. Shearing, S. J. Harris, N. P. Brandon, and V. Schmidt, "Stochastic simulation model for the 3D morphology of composite materials in li–ion batteries," *Computational Materials Science*, vol. 50, no. 12, pp. 3365–3376, 2011.
[41] D. Jeulin, "Random texture models for material structures," *Statistics and Computing*, vol. 10, no. 2, pp. 121–132, 2000.
[42] K. K. Lindfors, J. M. Boone, T. R. Nelson, K. Yang, A. L. Kwan, and D. F. Miller, "Dedicated breast CT: Initial clinical experience 1," *Radiology*, vol. 246, no. 3, pp. 725–733, 2008.
[43] T. Almecija, "Development of an anthropomorphic software model of the female breast," master thesis, Ecole Supérieure d'Electricité, 2015.
[44] M. Caballo, J. M. Boone, R. Mann, and I. Sechopoulos, "An unsupervised automatic segmentation algorithm for breast tissue classification of dedicated breast computed tomography images," *Medical physics*, vol. 45, no. 6, pp. 2542–2559, 2018.
[45] S. N. Chiu, D. Stoyan, W. S. Kendall, and J. Mecke, *Stochastic geometry and its applications*. John Wiley & Sons, 2013.
[46] E. W. Weisstein, "Euler angles," *https://mathworld. wolfram. com/*, 2009.
[47] I. Reiser, S. Lee, and R. Nishikawa, "On the orientation of mammographic structure," *Medical Physics*, vol. 38, no. 10, pp. 5303–5306, 2011.
[48] Z. Li, *Task-based optimization of 3D breast x-ray imaging using mathematical observers*. PhD thesis, Université Paris-Saclay (ComUE), 2017.
[49] A. Baddeley, I. Bárány, and R. Schneider, "Spatial point processes and their applications," *Stochastic Geometry: Lectures given at the CIME Summer School held in Martina Franca, Italy, September 13–18, 2004*, pp. 1–75, 2007.
[50] J. Møller and R. P. Waagepetersen, "Modern statistics for spatial point processes," *Scandinavian Journal of Statistics*, vol. 34, no. 4, pp. 643–684, 2007.
[51] F. Lafarge, G. Gimel farb, and X. Descombes, "Geometric feature extraction by a multimarked point process," *IEEE transactions on pattern analysis and machine intelligence*, vol. 32, no. 9, pp. 1597–1609, 2010.
[52] X. Descombes, R. Minlos, and E. Zhizhina, "Object extraction using a stochastic birth-and-death dynamics in continuum," *Journal of Mathematical Imaging and Vision*, vol. 33, no. 3, pp. 347–359, 2009.
[53] E. Lutwak, D. Yang, and G. Zhang, "A new ellipsoid associated with convex bodies.," *Duke Mathematical Journal*, vol. 104, no. 3, pp. 375–390, 2000.
[54] M. Ludwig, "Ellipsoids and matrix-valued valuations," *Duke Mathematical Journal*, vol. 119, no. 1, pp. 159–188, 2003.
[55] T. A. Sorensen, "A method of establishing groups of equal amplitude in plant sociology based on similarity of species content and its application to analyses of the vegetation on danish commons," *Biol. Skar.*, vol. 5, pp. 1–34, 1948.
[56] J. Illian, A. Penttinen, H. Stoyan, and D. Stoyan, *Statistical analysis and modelling of spatial point patterns*, vol. 70. John Wiley & Sons, 2008.
[57] A. Baddeley and R. Turner, "Spatstat: an R package for analyzing spatial point patterns," *Journal of statistical software*, vol. 12, no. 6, pp. 1–42, 2005.
[58] A. Baddeley, P. J. Diggle, A. Hardegen, T. Lawrence, R. K. Milne, and G. Nair, "On tests of spatial pattern based on simulation envelopes," *Ecological Monographs*, vol. 84, no. 3, pp. 477–489, 2014.
[59] R. B. Millar, *Maximum likelihood estimation and inference: with examples in R, SAS and ADMB*. John Wiley & Sons, 2011.
[60] F. J. Massey Jr, "The kolmogorov-smirnov test for goodness of fit," *Journal of the American statistical Association*, vol. 46, no. 253, pp. 68–78, 1951.
[61] P. Milioni de Carvalho, *Low-dose 3D quantitative vascular X-ray imaging of the breast*. PhD thesis, University Paris 11, 2014.
[62] J. G. Mainprize, A. H. Tyson, and M. J. Yaffe, "The relationship between anatomic noise and volumetric breast density for digital mammography," *Medical Physics*, vol. 39, 2012.